Available online at www.sciencedirect.com

ScienceDirect

journal homepage: www.elsevier.com/locate/he

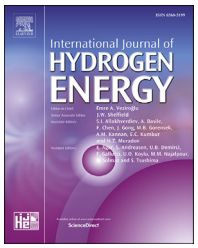

Modeling of the operation conditions on the gas purging performance of polymer electrolyte membrane fuel cells

Yu-Tong Mu, Pu He, Jing Ding, Wen-Quan Tao*

Key Laboratory of Thermo-Fluid Engineering and Science of MOE, School of Energy and Power Engineering, Xi'an Jiaotong University, Xi'an, Shaanxi, 710049, China

ARTICLE INFO

Article history:
Received 30 December 2016
Received in revised form
12 February 2017
Accepted 15 February 2017
Available online 18 March 2017

Keywords:
Polymer electrolyte membrane fuel cell
Gas purge
Two-fluid model
High frequency resistance
Liquid saturation

ABSTRACT

Gas purging has been a common and favorable strategy to improve the cold-start possibility of a polymer electrolyte membrane fuel cell (PEMFC). In the present study, water removal processes in a PEMFC during the gas purging prior to its shutdown are numerically investigated with a transient two-fluid model. The dryness in the sub-regions of the PEMFC is analyzed. Effects of the operation conditions (such as the gas flow rate, relative humidity and temperature) are also explored. The results indicate that water removal processes are not sequential and the main drying mechanism in the porous medium is the surface evaporation under the pendular stage. The overall dryness highly depends on the inlet water flux other than the convective water flux under the same gas flow rate. The operation parameters have a significant impact on the overall drying performance in terms of the purging effectiveness and the energy consumption.

1. Introduction

In recently years much progress has been made on the applications of the polymer electrolyte membrane fuel cell (PEMFC), which is served as power source. For instance, the Toyota motor company, as one of the hydrogen fuel cell vehicles manufacturer, has released its latest vehicles of the Mirai in November 2015. Despite of the achievements, water management in PEMFC is still a crucial issue to simultaneously obtain high membrane proton conductivity and avoid the occurrence of water flooding [1]. This issue gets worse when the PEMFC operates in a subfreezing environment or in a dead-end anode mode. The former one is known as cold start. The residual water in the microporous layers can weaken the water storage capacity of the membrane [2–10] and thereby lower the cold-start possibility. Several cold start modes including the constant voltage, current and power, together with the catalytic hydrogen-oxygen reaction in both electrolytes have been elucidated [6–8], and it has been found that the power output could be greatly limited by the initial membrane water and membrane temperature. The latter one is aimed to improve the hydrogen utilization efficiency [11-17]. The accumulated water and nitrogen in the anode due to the back diffusion from the cathode can result in gas starvation and thus affect the performance. The performance drop can be effectively recovered with an optimum of the purging cycle and operating conditions [13–15]. Therefore, to delineate the residual water in the PEMFC is important and gas purging has been considered as an effective strategy.

* *Corresponding author.*
E-mail address: wqtao@mail.xjtu.edu.cn (W.-Q. Tao).
http://dx.doi.org/10.1016/j.ijhydene.2017.02.108

Nomenclature

a	water activity
A	area, m^2
c	molar concentration, mol m^{-3}
c_p	specific heat capacity, J kg^{-1} K^{-1}
D	mass diffusivity, m^2 s^{-1}
EW	equivalent weight of membrane, kg mol^{-1}
F	Faraday's constant, 96,487 kC $kmol^{-1}$
h	latent heat, J kg^{-1}
I	current density, A m^{-2}
j	reaction rate, A m^{-3}
j_0	volumetric exchange current density, A m^{-3}
k	thermal conductivity, W m^{-1} K^{-1}
K	permeability, m^2
$\dot{m}$	mass flow rate, kg s^{-1}
M	molecular weight, kg $kmol^{-1}$
n_d	electro-osmotic drag coefficient
P	pressure, Pa
Q	volumetric flow rate, m^3 s^{-1}
R	universal gas constant, 8314 J $kmol^{-1}$ K^{-1}
s	liquid water saturation
t_{mem}	membrane thickness, m
t_{purge}	purge time, s
T	temperature, K
u	velocity, m s^{-1}
V	volume, m^3, or electrical potential, V
W	pumping power, W
X	molar fraction
α	transfer coefficient
γ	phase change rate coefficient, s^{-1}
ε	porosity
η	overpotential, V
θ	contact angle, °
κ	conductivity, S m^{-1}
λ	water content in ionomer
μ	dynamic viscosity, kg m^{-1} s^{-1}
ζ	stoichiometry ratio
ξ	membrane water variation
ρ	density, kg m^{-3}
σ	surface tension, N m^{-1}
ϕ	electronic potential, V
ω	volume fraction of ionomer

Abbreviations

AGC	Anode gas channel
ABP	Anode bipolar plate
AGDL	Anode gas diffusion layer
ACL	Anode catalyst layer
CGC	Cathode gas channel
CBP	Cathode bipolar plate
CGDL	Cathode gas diffusion layer
CCL	Cathode catalyst layer
HFR	High frequency resistance
MEM	Membrane
RH	Relative humidity

Subscripts and superscripts

a	anode
act	activation
amb	ambient
c	cathode
ch	channel
cond	condensation
EC	Energy consumption
eff	effective
ele	electronic
equil	equilibrium
f	fluid phase
hydr	hydronium
in	inlet
ion	ionic
k	species
m	mass
max	maximum
min	minimum
mw	membrane water
pc	phase change
pore	pore
rev	reversible
s	solid phase
sat	saturation
vl	vapor to liquid water
vp	vapor
w	water
wd	liquid water or vapor to membrane water

To date, an increasing effort has been made to reveal the complicated water transport mechanisms in the PEMFC. According to Cho and Mench [18–20], the water removal characteristics are controlled by the coupled effects of the surface evaporation and capillary flow in the porous medium (such as the gas diffusion layer (GDL) and catalyst layer (CL)), and following regimes can be identified: a surface evaporation regime, a constant rate period regime and a falling rate period regime. The first two regimes where the capillary driven flow dominates are called funicular stage, while the falling rate period regime where the vapour evaporation dominates is termed as pendular stage [20–24]. The constant rate period regime may not be observed if the porous medium is pure hydrophobic according to the experimental investigation by Shahidzadeh-Bonn et al. [25]. By comparing the effect of the material property on the competing phenomena of the water removal in porous medium, Cho and Mench [19] concluded that the capillary flow in porous medium dominants for carbon cloth with the liquid saturation above 0.09 and for paper-type with the liquid saturation above 0.12.

A thorough understanding on the effect of gas purging on the different sub-regions of the PEMFC is important to avoid the membrane degradation, reduce the parasitic power and guarantee the cold-start possibility. Some researchers [22,24] assumed that the overall dryness in different sub-regions of PEMFC is sequential. Starting from the gas channel (GC), then

GDL, CL and finally to membrane (MEM), the drying process can be divided into two steps. The first step refers to the water removal in CL and the second step is the water removal in MEM [26,27]. Based on such understanding, Sinha and Wang [22] developed an analytical purge model to describe CL/GDL and MEM drying for the cathode. Ito et al. [28] numerically studied the relationship between the purging time and gas flow rate. Ding et al. [29] extended the model of Sinha and Wang [22] by considering the adsorption and desorption of the membrane water and further proposed a gas purging strategy. Cho and Mench [19] pointed out that the above assumption was not appropriate since the water removal would directly from MEM with a high gas flow rate. Sinha and Wang [23] further presented a simplified isotherm two-mixture model to describe the water removal processes during the gas purging. However, the difference between the numerical and experimental results under lower temperatures was observed. They attributed it to the drying front morphology. Recently, Jiang and Wang [30] extended the two-mixture model to GCs and pointed out that the accumulation and transport mechanisms of liquid water in the anode and cathode channels were different.

Extensive experimental work has been devoted to understand the influence of the gas purging. Ge and Wang [2] explored the influence of the gas purging on the cold-start, and found that the gas purging was crucial to ensure the possibility of self-start. Hou et al. [31] investigated the effect of water removal on the performance of PEMFC after purging by the reactant gas. They found that no performance degradation was caused when the membrane water content in MEM reduced to an extent. St-Pierre et al. [5] found that progressive performance losses were observed after successive freeze/thaw cycles when purged with high temperature and they attributed them to the mass transport. Lee et al. [32] experimentally studied several factors of gas purging on the water removal in a short stack. The results suggested that the water removal rate decreased with purging time and the gas flow rate was more important than the purging time. Tajiri et al. [24] adopted two kinds of purge gases (nitrogen and helium) in their experimental work to study the purge effectiveness under different purge temperatures, gas flow rates and relative humidities. They found that the purging performance can be described by two parameters, namely the diffusive flux of water vapour across CL/GDL and the convective flux of water along the channel; helium is superior over nitrogen for the water removal due to its higher water diffusivity. Cho and Mench [18] developed an ex-situ gas purging test method for the water removal and proposed an efficient purge protocol to reduce the membrane moisture gradient and to reach the lowest liquid saturation level. Recently, Kim et al. [33] proposed a pressure reduction purge method to remove the residual water in CL/GDL within a limited time without significant durability degradation.

From the above brief review it can be seen that the water removal processes during the gas purging is very complicated, including the mass transfer among the membrane water in the ionomer, the liquid water in porous medium and the water vapour in both channels and porous medium. In order to simulate such complicated processes a more comprehensive model is needed. The gas purging is actually a two-phase flow in porous medium with physicochemical process. Thus in this paper, a transient two-fluid model for two-phase flow [34–37] has been adopted to investigate the influence of several operation factors on the overall water removal processes. The rest of the paper is organized as follows. First, a detailed description of the present gas purging model is presented. The model is validated with the experimental work afterwards. Subsequently, several factors influencing the water removal process and the purging effectiveness are discussed. Finally, some conclusions are made.

Model development

Simulation is conducted for one typical unit of a PEMFC, and the computation domain and its mesh system are illustrated in Fig. 1. The domain contains the whole components such as the bipolar plates (BPs), GCs, GDLs, CLs and MEM. The detailed geometric parameters and material properties are listed in Table 1. When the fuel cell works under the reaction mode, the cell operates at 343 K with the fully humidified hydrogen and air fed to the anode and cathode channels, respectively. The current density is set as 1 A cm^{-2} with the stoichiometry ratios of both electrodes of 2. When it works under the gas purging mode, the humidified nitrogen is fed to both electrodes. Inlet operating pressures for both electrodes for different modes are set as 1 atm. Table 2 lists the details of simulated cases with different operation conditions.

Governing equations

The present model considers all transient transport and physicochemical processes in PEMFC, which includes the conservations of mass, momentum, species, energy, charge, liquid water and dissolved water. Main assumptions are summarized as follows: (1) The gaseous mixture follows the ideal gas law [23,29,30,34,36,37]; (2) All the porous mediums are homogeneous and the contact resistances between different layers are ignored, which was often employed in previous modelling work [6,23,30,36]; (3) The amount of liquid water saturation in both gas channels is fixed as zero, because the liquid water can be removed fast due to the high velocity of inlet gases and the short straight channels [8,29,36]; (4) The water produced from the electrochemical reaction is in liquid phase since the gases are fully humidified [35,36]. All the conservation equations are briefly described as follows [1].

Mass of gaseous mixture:

$$\frac{\partial}{\partial t}\left(\varepsilon_{\mathrm{eff}}\rho_{\mathrm{g}}\right)+\nabla\cdot\left(\rho_{\mathrm{g}}u_{\mathrm{g}}\right)=S_{\mathrm{m}} \tag{1}$$

Momentum of gaseous mixture:

$$\frac{\partial}{\partial t}\left(\frac{\rho_{\mathrm{g}}u_{\mathrm{g}}}{\varepsilon_{\mathrm{eff}}}\right)+\nabla\cdot\left(\frac{\rho_{\mathrm{g}}u_{\mathrm{g}}u_{\mathrm{g}}}{\varepsilon_{\mathrm{eff}}^{2}}\right)=-\nabla p_{\mathrm{g}}+\mu_{\mathrm{g}}\nabla\cdot\left(\nabla\left(\frac{u_{\mathrm{g}}}{\varepsilon_{\mathrm{eff}}}\right)+\nabla\left(\frac{u_{\mathrm{g}}^{\mathrm{T}}}{\varepsilon_{\mathrm{eff}}}\right)\right)-\frac{2}{3}\mu_{\mathrm{g}}\nabla\left(\nabla\cdot\left(\frac{u_{\mathrm{g}}}{\varepsilon_{\mathrm{eff}}}\right)\right)+S_{\mathrm{u}} \tag{2}$$

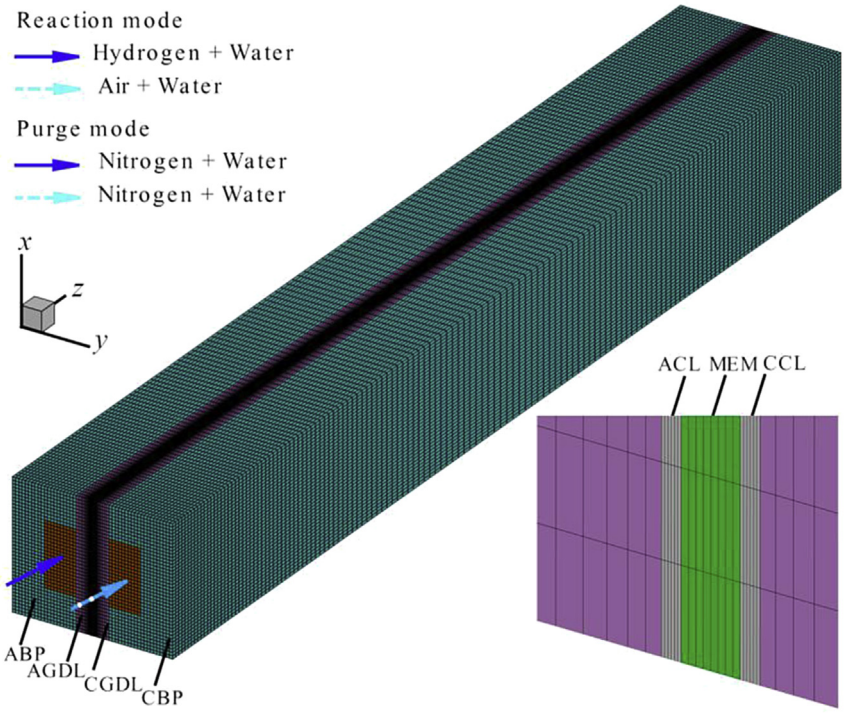

Fig. 1 – Computational domain and the mesh system

Table 1 – Geometric parameters and material properties [23,37].

Parameter	Value
Gas channel width/depth	1.0/0.5 mm
Bipolar plate width	1.0 mm
GDL thickness	0.23 mm
CL thickness	0.01 mm
MEM thickness	0.03 mm
Porosity of GDL/ CL,ε	0.6/0.6
Permeability of GDL/CL,K_{GDL}/K_{CL}	$4.0 \times 10^{-12}/4.0 \times 10^{-12}$ m^2
Contact angle of GDL/CL,θ	110°/110°
Heat capacity of MEM/GDL/CL/BP,c_p	833/3300/568/1580 J kg^{-1} K^{-1}
Heat conductivity of MEM/GDL/CL/BP,κ_s	0.95/1.0/1.0/20 W m^{-1} K^{-1}
Electronic conductivity of GDL/CL/BP,σ_{ele}	750/750/20000 S m^{-1}
Equivalent weight, EW	1.1 kg mol^{-1}
Density of dry MEM,ρ_{MEM}	1980 kg m^{-3}

Table 2 – Simulated cases with different operation conditions.

Description	Gas temperature (K)	Gas relative humidity (%)	Gas flow rate (10^{-6} m^3 s^{-1})
Basic case	343	50	3.74
Case 1	343	50	0.935, 1.87, 7.48, 14.96
Case 2	343	10, 30, 70, 90	3.74
Case 3	323, 333, 353	50	3.74

Gas species transport:

$$\frac{\partial}{\partial t}\left(\varepsilon_{\text{eff}}\rho_g X_k\right) + \nabla\cdot\left(\rho_g u_g X_k\right) = \nabla\cdot\left(\rho_g D_k^{\text{eff}}\nabla X_k\right) + S_k \quad (3)$$

Electronic potential transport:

$$0 = \nabla\cdot\left(\kappa_{\text{ele}}^{\text{eff}}\nabla\phi_{\text{ele}}\right) + S_{\text{ele}} \quad (4)$$

Ionic potential transport:

$$0 = \nabla\cdot\left(\kappa_{\text{ion}}^{\text{eff}}\nabla\phi_{\text{ion}}\right) + S_{\text{ion}} \quad (5)$$

Liquid water transport:

$$\frac{\partial}{\partial t}(\varepsilon s\rho_l) + \nabla\cdot\left(\rho_l\frac{\mu_g}{\mu_l}\frac{K_l}{K_g}u_g\right) = \nabla\cdot(\rho_l D_c\nabla s) + S_{\text{liq}} \quad (6)$$

Dissolved water transport:

$$\frac{\rho_{\text{mem}}}{EW}\frac{\partial}{\partial t}(\omega\lambda) = \frac{\rho_{\text{mem}}}{EW}\nabla\cdot\left(D_{\text{mw}}^{\text{eff}}\nabla\lambda\right) + S_{\text{mw}} \quad (7)$$

Energy transport:

$$\frac{\partial}{\partial t}\left(\left(\rho c_p\right)_{f,s}^{\text{eff}}T\right) + \nabla\cdot\left(\left(\rho c_p u\right)_{f,s}^{\text{eff}}T\right) = \nabla\cdot\left(k_{f,s}^{\text{eff}}\nabla T\right) + S_T \quad (8)$$

Detailed explanations on all the above equations are presented as follows. Note that all the above equations are coupled with each other through the source terms, which are related with the electrochemical reactions or the conversions among different kinds of water states through the interfacial mass transfer. The expressions for all the source terms are listed in Table 3. The effective mass diffusion coefficient D_k^{eff} is related with the bulk diffusivity D_k according to the Bruggeman correlation

Table 3 – Source terms for all the conservation equations [1].

Equations	Source term expressions
Mass	$S_m = S_{H_2} + S_{O_2} + S_{vp}$
Momentum	In GDL/CL:$S_u = -\frac{\mu_g}{K_{GDL/CL}} u_g$
Species	In ACL, $S_{H2} = -\frac{j_a}{2F} M_{H_2}$; in CCL, $S_{O2} = -\frac{j_c}{4F} M_{O2}$; in GDL/CL, $S_{vp} = -S_{vl}$
Electronic potential	In ACL, $S_{ele} = -j_a$; in CCL, $S_{ele} = j_c$
Ionic potential	In ACL, $S_{ion} = j_a$; in CCL, $S_{ion} = -j_c$
Liquid water	In ACL,$S_{liq} = S_{vl} - M_{H_2O} S_{wd}$; in CCL, $S_{liq} = \frac{j_c}{4F} M_{H2O} + S_{vl} - M_{H_2O} S_{wd}$; in GDL, $S_{liq} = S_{vl}$
Dissolved water	In CLs, $S_{mw} = S_{wd} + S_{EOD}$
Energy	In BP,$S_T = \sigma_{ele}^{eff} \|\nabla\phi_{ele}\|^2$; in GDL,$S_T = \sigma_{ele}^{eff} \|\nabla\phi_{ele}\|^2 + S_{pc}$; in ACL, $S_T = j_a \|\eta_{act}\| + \sigma_{ele}^{eff} \|\nabla\phi_{ele}\|^2 + \sigma_{ion}^{eff} \|\nabla\phi_{ion}\|^2 + S_{pc}$; in CCL, $S_T = -\frac{j_c T \Delta S}{2F} + j_c \|\eta_{act}\| + \sigma_{ele}^{eff} \|\nabla\phi_{ele}\|^2 + \sigma_{ion}^{eff} \|\nabla\phi_{ion}\|^2 + S_{pc}$; in MEM, $S_T = \sigma_{ion}^{eff} \|\nabla\phi_{ion}\|^2$

$$D_k^{eff} = \varepsilon_{eff}^{1.5} D_k \tag{9}$$

The effective electron conductivity κ_{ele}^{eff} and ion conductivity κ_{ion}^{eff} in the electronic and ionic conservation equations are affected by the porosity and the electrolyte volume fraction ω as follows [36]

$$\kappa_{ele}^{eff} = (1 - \varepsilon - \omega)^{1.5} \kappa_{ele} \tag{10}$$

$$\kappa_{ion}^{eff} = \omega^{1.5} \kappa_{ion} \tag{11}$$

Following the work by Refs. [23,29,38], the GORE-SELECT membrane is chosen with its conductivity κ_{ion} expressed as

$$\kappa_{ion} = \frac{1}{2}(0.5139\lambda - 0.326)\exp\left[1268\left(\frac{1}{303} - \frac{1}{T}\right)\right] \tag{12}$$

The electrochemical reaction rates in both catalyst electrodes are calculated with a corrected Butler–Volmer equation with the liquid blockage considered [1]

$$j_a = (1 - s) j_{0,a}^{ref} \left(\frac{c_{H_2}}{c_{H_2}^{ref}}\right)^{0.5} \left[\exp\left(\frac{2\alpha_a F}{RT}\eta_{act}\right) - \exp\left(-\frac{2\alpha_c F}{RT}\eta_{act}\right)\right] \tag{13}$$

$$j_c = (1 - s) j_{0,c}^{ref} \frac{c_{O_2}}{c_{O_2}^{ref}} \left[-\exp\left(\frac{4\alpha_a F}{RT}\eta_{act}\right) + \exp\left(-\frac{4\alpha_c F}{RT}\eta_{act}\right)\right] \tag{14}$$

$$\eta_{act} = \phi_{ele} - \phi_{ion} \tag{15}$$

All the related electrochemical parameters and physical properties are listed in Table 4.

The gas phase permeability K_g and the liquid phase permeability K_l in Eq. (6) are related with the intrinsic permeability of the porous medium K_0 and liquid saturation S as $K_g = K_0(1 - s)^4$ and $K_l = K_0 s^4$, respectively [36]. The liquid water diffusivity D_c is expressed as

$$D_c = -\frac{K_g}{\mu_l}\frac{dp_c}{ds} \tag{16}$$

where the capillary pressure p_c is calculated as a function of s with the Leverett-J function as follows [39]

Table 4 – Model parameters and physical properties [36,37].

Parameter	Value
Hydrogen/oxygen diffusivity,D_{H_2}/D_{O_2}	$0.915/0.22 \times 10^{-4}$ m^2 s^{-1}
Water diffusivity,D_{H_2O}	0.256×10^{-4} m^2 s^{-1}
Surface tension,σ	0.0625 N m^{-1}
Latent heat of vapor condensation,h_{cond}	2.395×10^6 J kg^{-1}
Latent heat of hydronium,h_{hydr}	3.462×10^6 J kg^{-1}
Entropy change of reaction, ΔS	-163110 J kmol^{-1} K^{-1}
Dimensionless phase transfer rates, $Sh_{cond/evap}$	2.04×10^{-3}
Pore surface area, A_{pore}	2.0×10^5 m^{-1}
Characteristic length, d	5.0×10^{-6} m
Phase change rate coefficient,γ_{ld}	1.0 s^{-1}
Volume fraction of ionomer in CL,ω	0.22
Anode/cathode exchange current density multiplied by specific area,$j_{0,a}^{ref}/j_{0,c}^{ref}$	$5 \times 10^7/120$ A m^{-3}
Reference hydrogen/oxygen concentration,$c_{H2}^{ref}/c_{O2}^{ref}$	56.4/3.39 mol m^{-3}
Anodic/cathodic transfer current,α_a/α_c	0.5/0.5

$$p_c = \sigma\cos\theta\left(\frac{\varepsilon}{K_0}\right)J(s) \tag{17}$$

$$J(s) = \begin{cases} 1.42(1-s) - 2.12(1-s)^2 + 1.26(1-s)^3 & \theta < 90^\circ \\ 1.42s - 2.12s^2 + 1.26s^3 & \theta > 90^\circ \end{cases} \tag{18}$$

where σ is the surface tension between vapour and liquid phases and θ is the contact angle characterizing the wettability of the porous material. The source term S_{vl} in Table 3 denotes the interfacial mass transfer between the liquid and vapour state due to evaporation or condensation and can be calculated with the Langmuir type equation [1]

$$S_{vl} = \begin{cases} A_{pore}\dfrac{Sh_{cond} D_{H_2O}}{d}\varepsilon(1-s)\dfrac{(p_{vp} - p_{sat})}{RT} & \text{if } p_{vp} \geq p_{sat} \\ A_{pore}\dfrac{Sh_{evap} D_{H_2O}}{d}\varepsilon s\dfrac{(p_{vp} - p_{sat})}{RT} & \text{if } p_{vp} < p_{sat} \end{cases} \tag{19}$$

The saturation pressure p_{sat} is provided by the following expression [40]:

$$\log_{10}\left(\frac{p_{sat}}{101325}\right) = -2.1794 + 0.02953(T - 273.15) - 9.1837 \times 10^{-5}(T - 273.15)^2 + 1.4454 \times 10^{-7}(T - 273.15)^3 \quad (20)$$

The transport equation for dissolved water λ (the number of water molecules per sulfonic acid group within the membrane) considers the membrane water adsorption/desorption process in CLs. The mass transfer rate S_{wd} between the membrane water and vapour in pores is determined as [34]

$$S_{wd} = \gamma_{wd}\frac{\rho_{mem}}{EW}(\lambda - \lambda_{equil}) \quad (21)$$

where the equilibrium membrane water content

λ_{equil} is expressed as a function of the water activity a [40]

$$\lambda_{equil} = \begin{cases} 0.043 + 17.18a - 39.85a^2 + 36a^3 & (0 < a < 1) \\ 14 + 1.4(a - 1) & (1 \le a \le 3) \end{cases} \quad (22)$$

$$a = \frac{p_{vp}}{p_{sat}} + 2s \quad (23)$$

Due to the impact of electro-osmotic drag (EOD), water in the anode can be dragged to cathode by the hydrogen ions; therefore, the source term S_{EOD} is added into the membrane water conservation equation:

$$S_{EOD} = \begin{cases} \frac{n_d j_a M_{H2O}}{F} & \text{in anode CL} \\ -\frac{n_d j_c M_{H2O}}{F} & \text{in cathode CL} \end{cases} \quad (24)$$

where n_d is the drag coefficient and it is expressed as [40]

$$n_d = \frac{2.5\lambda}{22} \quad (25)$$

The membrane water diffusivity is estimated with the following equation [40]

$$D_w = 2.1 \times 10^{-7}\exp(-2346/T)\lambda \quad (26)$$

In the energy conservation equation, the effective volumetric heat capacity and thermal conductivity are obtained with a volume averaged method [3]:

$$(\rho c_p)^{eff}_{f,s} = \varepsilon\left(s(\rho c_p)_l + (1 - s)(\rho c_p)_g\right) + (1 - \varepsilon)(\rho c_p)_s \quad (27)$$

$$k^{eff}_{f,s} = \varepsilon\left(sk_l + (1 - s)k_g\right) + (1 - \varepsilon)k_s \quad (28)$$

The source term in Eq. (8) includes the reversible heat, activation heat, Ohmic heat and latent heat. The latent heat is expressed as:

$$S_{pc} = \begin{cases} h_{cond}S_{vl} & \text{in GDLs} \\ h_{cond}S_{vl} - h_{hydr}S_{wd}M_{H2O} & \text{in CLs} \end{cases} \quad (29)$$

where h_{cond} is the condensation latent heat, and h_{hydr} refers to the latent heat of hydronium due to the adsorption/desorption of the membrane water [41].

Boundary and initial conditions

In order to study the water transport in the fuel cell under the purge mode, an initial water distribution of different water states is needed. Following the work of [23], the initial condition for the purge mode is based on a steady-state simulation of the reaction mode. It is worth noting that the charge transport equations Eqs. (4) and (5) are only solved in the reaction mode. The detailed boundary conditions for the reaction mode are as follows:

At the channel inlets, the mass flow rates are specified by

$$\dot{m}_a = \varsigma_a\frac{p_{a,in}}{RT_{in}}\frac{I_{ref}A_{act}}{2c_{H2,in}}, \quad \dot{m}_c = \varsigma_c\frac{p_{c,in}}{RT_{in}}\frac{I_{ref}A_{act}}{4c_{O2,in}} \quad (30)$$

$$c_{H2,in} = \frac{p_{a,in} - RH_a p_{sat}}{RT_{in}}, \quad c_{O2,in} = \frac{0.21\left(p_{c,in} - RH_c p_{sat}\right)}{RT_{in}} \quad (31)$$

The inlet temperature T_{in} equals to the operation temperature.

At the channel outlets, constant pressures are defined (1 atm.).

At the outer surface of the CBP, a reference electronic potential (zero) is set; while at the outer surface of the ABP, a constant flux (current density) is applied,

$$-\kappa_{ele}\frac{\partial\phi_{ele}}{\partial y} = I_{ref} \quad (32)$$

At the outer surfaces along the x-direction, symmetry boundary condition is imposed. No-slip boundary condition is employed for all velocities on the solid walls, and zero-flux boundary condition is applied on all external boundaries for the transport scalars in Eqs. (3–8) if not specially described.

From above governing equations and boundary conditions, the electronic potential on the outer surface of the ABP φ can be solved, then the output voltage V_{cell} is obtained as follows,

$$V_{cell} = V_{rev} - \varphi \quad (33)$$

where V_{rev} refers to the reversible voltage of the fuel cell and is determined by

$$V_{rev} = 1.229 - 0.846 \times 10^{-3}(T_0 - 298.15) + \frac{RT_0}{2F}\left(\ln p^{in}_{H_2} + \frac{1}{2}\ln p^{in}_{O_2}\right) \quad (34)$$

where $p^{in}_{H_2}$ and $p^{in}_{O_2}$ are the inlet partial pressures of hydrogen and oxygen, respectively.

After the fuel cell operating under the reaction mode reaches a steady state, the purge mode starts. Only the boundary conditions for the channel inlets are changed as follows:

The velocities are specified as

$$u_{in,a} = Q_a/A_{ch}, \quad u_{in,c} = Q_c/A_{ch} \quad (35)$$

The purging temperature is defined according to Table 2. The inlet mass fractions are related with the inlet pressure and relative humidity.

Numerical procedure

All the conservation equations are solved in the commercial CFD software FLUENT based on finite volume method. All the physical properties, source terms and scalars (such as ϕ_{ele}, ϕ_{ion}, s and λ_{mf}) in the governing equations are implemented with the user-defined functions (UDF). The convection and diffusion terms are discretized by the QUICK scheme and the second-order central difference scheme, respectively. The iteration process at each time step will not be terminated until the maximum residual is less than 10^{-8}. Grid-independent tests for the steady reaction mode were performed along three different directions, and it was found that the result was much more sensitive to the grid number along the y-direction (thickness direction) compared with that along the other two directions. Four different mesh systems thus were designed only by altering the grid numbers along the y-direction. The critical parameters such as the output voltage, the average temperature and the high frequency resistance (HFR, see Eq. (36)) of membrane were compared in Fig. 2. It can be seen that the meshing system with the total number of computational grid of 504, 000 was sufficient to obtain the grid-independent results.

Validation of the model

To verify the present model, the volumetrically averaged HFR is adopted as an indicator to monitor the status of the membrane water content in MEM, and which is calculated with the following equation:

$$\frac{t_{mem}}{HFR} = \frac{1}{V_{mem}} \int \frac{1}{\kappa_{ion}^{eff}} dV_{mem} \tag{36}$$

where t_{mem} and V_{mem} refer to the thickness and volume of MEM, respectively.

The evolution of the HFR predicted by the present model has been compared with the experiment conducted by Tajiri et al. [24] and the numerical result studied by Sinha and Wang [23]. The operation condition in the validation work is consistent with that in the above two literature. The cell operates at 323 K with the fully humidified hydrogen and air under the pressure of 1 atm; the current density before the gas purging is 0.5 A cm^{-2} with the stoichiometry ratios for the anode and cathode electrolytes of 18 and 21, respectively; all the geometric and physical parameters are exactly the same. The results are presented in Fig. 3. It can be observed from the figure that the cell voltage predicted with the present model agrees quite well with the experimental data. The predicted evolution characteristics of the HFR are also consistent with the existing literature including the slow rise, fast rise and membrane equilibrium periods [22–24]. Dryness of the water vapour in GCs and the liquid water in GDLs occurs ahead of the membrane water desorption in CLs firstly; afterwards the conversion between the water in ionomer and the water vapour in CLs happens and results in an increasing variation of membrane water in MEM. The equilibration of the membrane water with the relative humidity of the purging gas is finally achieved. In the present model the conversion of water in different states has been fully considered and non-isotherm simulation was conducted, thus the agreement of the present results with test data has been very much improved.

Results and discussions

In this section, we will present the results of parameter sensitivity studies to examine the effects of purging gas flow rate, temperature and relative humidity on the water removal process and the purging performance. Main focus is put on the dryness of GCs, GDLs, CLs and MEM. It should be pointed out that the purging process is initiated by the steady state of the reaction mode. Detailed simulated cases are listed in Table 2.

Characteristics of the dryness process of the base case

Attention is firstly turned to the dryness of GCs. Fig. 4 presents the time evolution of the relative humidity at the central lines of GCs. The x-axis is normalized by the channel length. The average inlet velocity of the purging gas is 7.44 m s^{-1} with its corresponding Reynolds number of 280. Therefore, it only takes about 0.007 s for the purging gas to reach the outlet and hence the relative humidity decreases fast. The relative

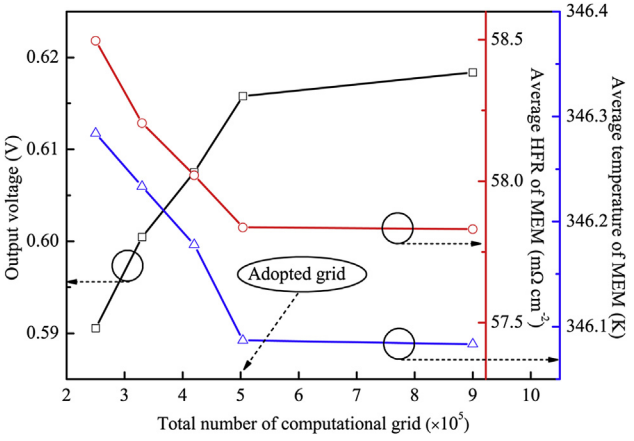

Fig. 3 – Comparison of the membrane HFR between numerical results and experimental result

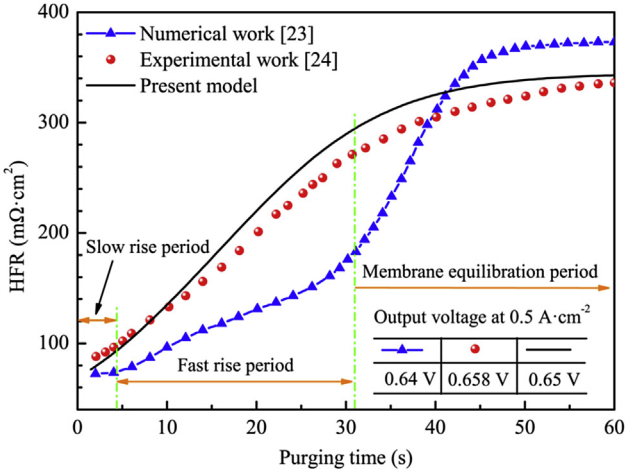

Fig. 2 – Grid-independent study for the variations of different parameters

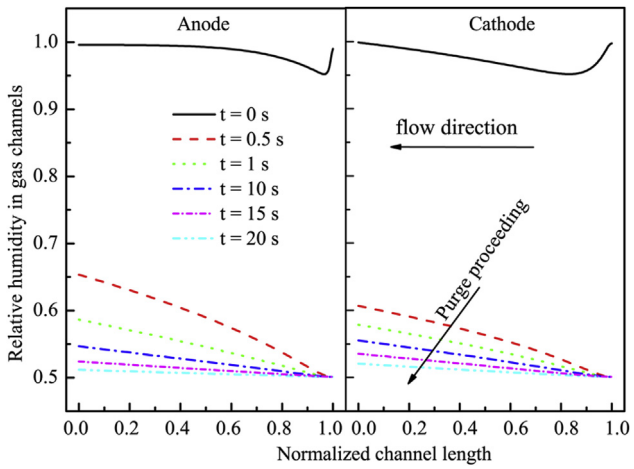

Fig. 4 – Time evolution of the relative humidity at the central line of the channels

humidity at t = 0 refers to the water distribution in GCs at the steady state. At this instant, along the flow direction, the relative humidity decreases firstly and then increases. This is because the average temperature in the outlet is about 1 K higher than that in the inlet and it results in 1550 Pa higher of the water saturation pressure according to Eq. (20). Besides, the temperature in the cathode is a little higher than that in anode, which explains slightly lower relative humidity in CGC for the first several seconds. As the purging proceeds, the relative humidity in CGC is relatively higher due to a larger evaporation flux from the cathode porous medium. Fig. 4 also displays that the relative humidity increases monotonically along the flow direction due to the accumulation of the purged water from the cell, and which agrees well with the result presented by Tajiri and Wang [23] qualitatively. The increasing relative humidity weakens the dryness ability along the flow direction. The time evolution of the relative humidity indicates that the rate of purged water mass flux decreases with time since the liquid saturation decreases.

The dryness process of the porous medium is depicted in Fig. 5. Before the gas purging, the volumetrically averaged liquid saturation of CCL is the highest due to the water

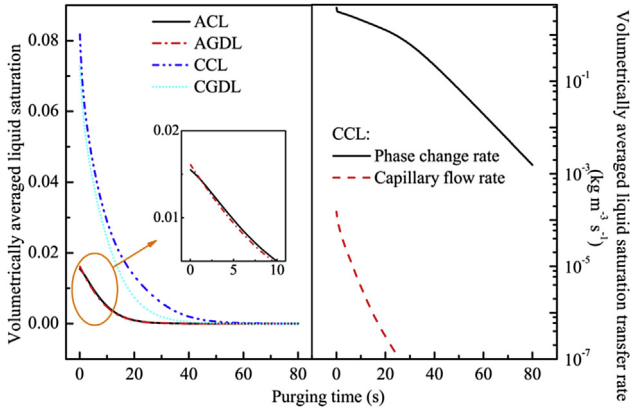

Fig. 5 – Time evolution of the volumetrically averaged liquid saturation and its transfer rate in the porous medium.

production and that of ACL is the lowest because of the impact of EOD. Liquid in GDLs can be purged much easier when compared with that in CLs as the drying front proceeds into GDLs firstly. However, this figure shows that the drying time needed to purge the liquid in GDLs/CLs thoroughly does not change much since the thickness of CLs is comparatively small. Besides, the liquid water removal process in GDLs/CLs occurs almost in the same time, which suggests that the dryness in the sub-regions of PEMFC is not all sequential. This figure also presents the evolution of the volumetrically averaged liquid saturation transfer rate. It can be found that the main drying mechanism in CCL is phase-change induced since the phase change rate is about 3 order magnitudes larger than the capillary flow rate. The capillary flow rate is obtained from the second term in the left hand of Eq. (6). This result indicates that the water removal process is in pendular stage and therefore the water removal rate decreases with the purging time throughout the whole drying process. This phenomenon has been revealed by both the experimental work [18,19,24,25] and the numerical studies [22,23].

Fig. 6 illustrates the evolution of liquid saturation distribution at two planes. It can be found that the drying front moves in the through-plane as the purging proceeds, which will increase the distance between the drying front and the interface of GC and GDL. Consequently, the purging rate of the liquid water decreases. When the purging time is higher than 15 s, it can be clearly observed that the liquid saturation under the anode channel has been removed thoroughly. Fig. 6(a) also shows that the dryness of GDL/CL is not sequential. The decreasing liquid saturation in CLs will result in the variation of the membrane water in CLs, which will promote the dryness of the membrane at the same time. This explains the sequential variation of membrane HFR with purging time observed in the experimental result [24]. Fig. 6(b) also shows that the liquid saturation underneath the rib is higher than that underneath the channel due to the difficulty to remove the water.

Fig. 7 presents the evolution of the membrane dryness. The volumetrically averaged temperature of the membrane drops dramatically as the purging starts. The reason can be explained as follows. The heat source terms (such as the reversible heat, activation heat, Ohmic heat) disappear as the cell shuts down, and only the heat sink of the latent heat due to the phase change and desorption of the membrane water exists. As shown in Fig. 5, the water removal rate due to the evaporation decreases as purging proceeds, causing the average temperature of membrane increases back to the purging temperature. Similar result has been found by Cho and Mench [20] in their experimentally study and they concluded that the maximum temperature drop was related with the purging flow rate. Fig. 7 also depicts the evolution of the volumetrically averaged membrane water content and HFR. The equilibrium membrane water content in CLs is proportional to the liquid saturation (see Eqs. (22, 23)), and thereby the variation of the membrane water content in membrane is similar to that of the liquid saturation shown in Fig. 5. The membrane proton conductivity is proportional to the membrane water, which explains that the variation of the HFR is contrary to that of the membrane water content. It is noted that the membrane water after gas purging is a critical

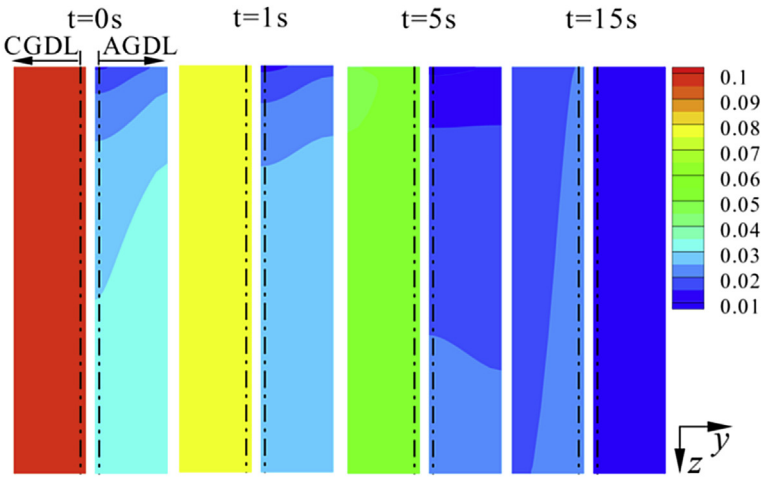

(a) Liquid saturation at the plane of x=0 (the ratio of length in z- and y- directions is 40)

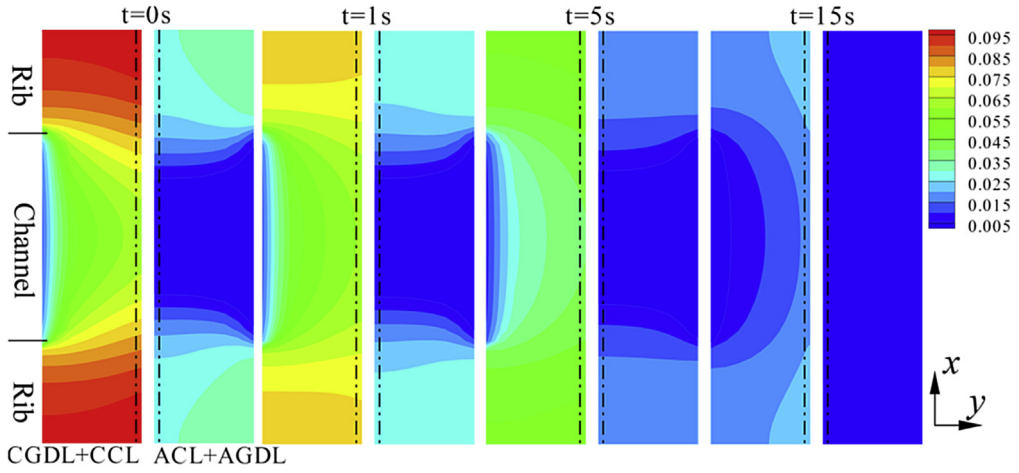

(b) Liquid saturation at the middle cross-section along the flow direction (the ratio of length in x- and y- directions is 2)

Fig. 6 – Liquid saturation distribution at time instants of 0, 1, 5 and 15 s. Only the sub-regions such as the CL and GDL are displayed

parameter determining the cold-start possibility. As is addressed by Wang et al. [4], there exist two critical membrane water content values, and above the higher one self-start is not possible with catalyst being engulfed with ice and below the lower one the self-start is achievable without forming ice. The membrane water after gas purging is highly affected by the operation conditions [1–4,10,24], and thus the influences of the operation conditions are explored in the following sections.

Fig. 8 illustrates the evolution of membrane water content distribution at two cross-sections. Along the flow direction, the membrane water increases due to the increasing relative humidity in channels. As the purging proceeds, the membrane water transforms into liquid/vapour with the desorption process in CLs (see Eq. (21)), which results in lower membrane water content in MEM. The membrane water in CCL is comparatively higher than that in ACL, and therefore the membrane water diffuses from cathode to anode during the gas purging. The membrane water under the rib is higher than that under the channel, which is corresponding to the liquid saturation distribution in porous medium.

In the following the influences of the gas flow rate, relative humidity and temperature will be presented in order.

Influence of the volumetric flow rate (case 1)

The volumetric flow rate is crucial since a trade-off should be achieved between the purging time and the purging effectiveness. The influence of the gas flow rate on the water removal attributes to two mechanisms: surface evaporation and motion of the liquid water. The surface evaporation rate is related with the Reynolds number and Schmidt number [42], while the liquid water movement is determined by the adhesion and drag forces [43]. As mentioned above, the

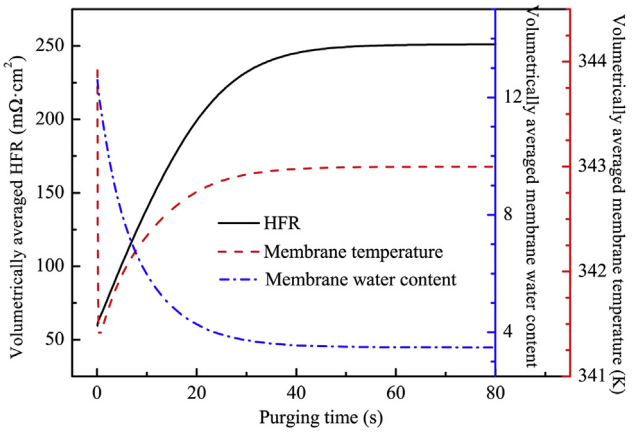

Fig. 7 – Time evolution of the volumetrically averaged HFR, membrane water content and temperature of MEM.

capillary effect can be ignored since the surface evaporation dominates the water removal in porous medium. The dryness of GCs is relatively fast compared with that of other sub-regions, and therefore we mainly focus on the dryness of the porous medium and membrane.

The time evolution of the averaged liquid water saturation in CLs with different gas flow rates has been depicted in Fig. 9. As expected, the increasing gas flow rate benefits the surface evaporation and also accelerates the diffusion of the water vapour. For example, when the average liquid saturation decreases to 0.01, the purging time needed for ACL/CCL is 6.3/27.8, 5.3/25.3, 4.7/23.9, 4.5/23.3 and 4.3/23.0 s with the gas flow rates of 0.96, 1.92, 3.84, 7.68 and 15.36 $\times$ 10^{-6} m^3 s^{-1}, respectively. However, as can be observed from the figure, the influence of the gas flow rate on the dryness of the CLs is not significant, which indicated that the water removal in CL is diffusion dominated. Similar result has been observed by Tajiri et al. [24]. The above result is a little different from the experiment result in Ref. [32] which stated that the flow rate was advantageous over purging time. This is mainly because the liquid droplet exists in the channels due to a higher initial liquid saturation; higher gas flow rate corresponding to higher stagnation pressure and thereby can push the droplet away physically.

Fig. 10 shows the evolution curves of the volumetrically average HFR and membrane water with different gas flow rates in MEM. As shown in the figure, HFR increases rapidly with purging time and then reaches a constant. Like the liquid water removal in porous medium, the gas flow rate does not show much influence on the evolution of the membrane water content. This is probably because the gas flow rate is sufficiently large, and therefore the HFR is only determined by the diffusion. Similar result has also been revealed by Tajiri et al. [24]. Following the work of Wang et al. [4], we choose the membrane water content of 6 as a critical value beyond which the cold-start is not possible. When the membrane water content reaches 6, the purging time is 14.5, 11, 9.9, 9 and 8.55 s for the gas flow rates of 0.96, 1.92, 3.84, 7.68 and 15.36 $\times$ 10^{-6} m^3 s^{-1}, respectively. It is indicated that the improvement of the overall dryness with higher gas flow rate is not encouraged. The final membrane water is around 3.5, which is independent on the gas flow rate. This result has also been found in Refs. [22,24,29]. Since the final membrane water is in equilibrium with the relative humidity of purging gas, the HFR therefore tends to approach the theoretic equilibrium membrane water content.

Influence of the relative humidity (case 2)

Purging with dry gas is supposed to be the simplest and most effective way for the water removal in the fuel cell by allowing more water to evaporate into the unsaturated gas [3,43]. However, steep water content gradients in membrane could easily result in the mechanical stress, which would lead to the degradation of MEM [20]. Therefore, it is essential to evaluate the performance of the purging gas with different relative humidities in terms of the purging efficiency and the uniformity of the membrane water distribution during its dryness.

Fig. 11 shows the evolution of liquid water with different purging RH in CLs. As expected, the purging time needed for the dryness of the CLs decreases with a lower RH. However, the effect of purging RH on the dryness for the cathode is relatively complicated even though the general variation trend is the same as for the anode, with the effect of RH being much less. This is because the evaporation and desorption rates for CCL are much higher than that for ACL due to its higher liquid saturation and membrane water content. It can be seen from this figure that during the time 0–10 s, the volumetrically averaged liquid saturation for CCL decreases with the decrease in purging relative humidity. This can be explained as follows. As is depicted in Fig. 12, the maximum volumetrically average membrane temperature drops are 5.2, 4.4, 3.4, 2.4 and 1.8 K for the relative humidity of 10%, 30%, 50%, 70% and 90%, respectively. The decreasing temperature in the porous medium benefits the water condensation. A trade-off between the evaporation and the decreasing temperature in CLs explains the tendency of liquid saturation evolution in CCL. It is also interesting to find that the volumetrically averaged liquid saturation with the purging relative humidity of 10% is slightly higher than that of 30% for CCL during the purging time of 20–60 s. Besides, it takes more time to purge CCL thoroughly with the relative humidity of 10% compared with that of 30%. This can be explained as follows. Most of the liquid water in GDLs has been removed before 20 s (see Fig. 5), and the equilibrium membrane water content decreases with the reduction of the relative humidity, indicating that more membrane water can be dragged from the MEM and CLs. For example, the final membrane water after gas purging with the relative humidity of 10% and 30% are 1.47 and 2.78, respectively. The desorbed membrane water transfers to the water vapor or liquid water (see Eq. (21)), which explains the aforementioned phenomena. Fig. 12 also indicates that the surface evaporation rate shows high dependence on the relative humidity in the most part of the purging process.

Fig. 13 illustrates the evolution of the volumetrically averaged HFR and the membrane water content. The dryness of the membrane shows significantly dependence on the purging relative humidity. It is interesting to note that the membrane water increases with the relative humidity of 90% for the first several seconds. This may be explained as follows. In

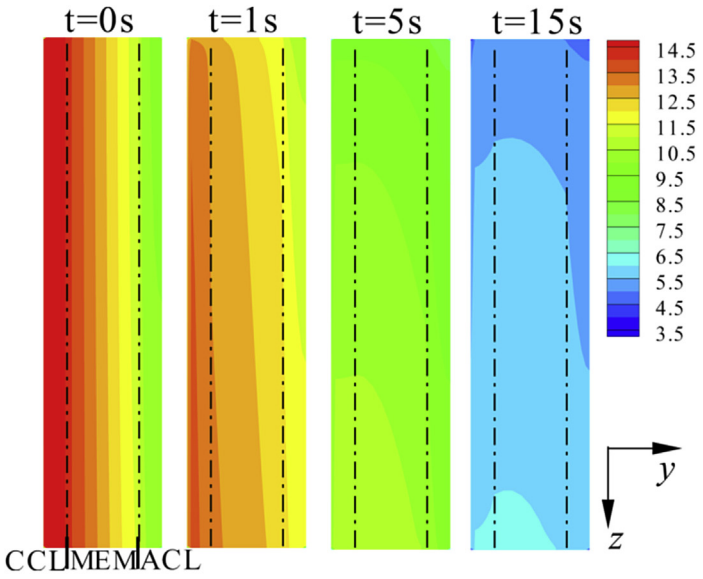

(a) Membrane water content at the plane of x=0 (the length ratio of z and y is 250)

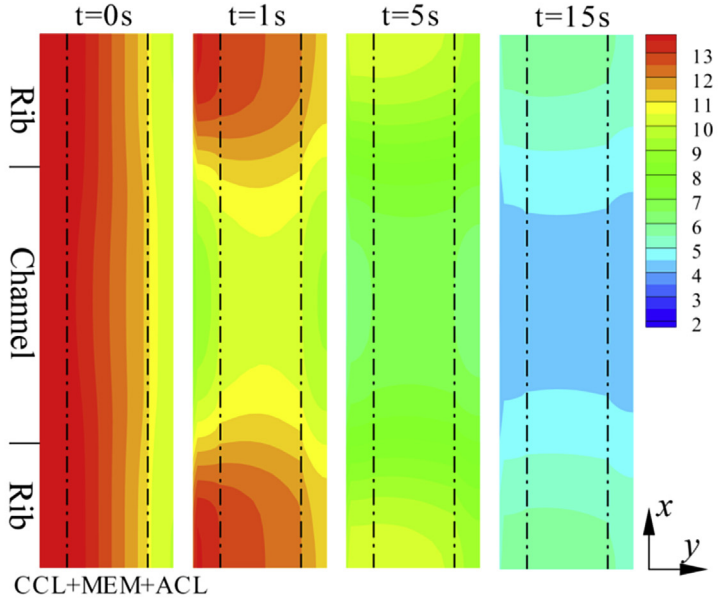

(b) Membrane water content at the middle cross-section along the flow direction (the ratio of length in x and y directions is 10)

Fig. 8 – Membrane water distributions of the basic case at time instants of 0, 1, 5 and 15 s. Only the sub-regions such as the CL and MEM are displayed

this simulation the inlet water fluxes for anode and cathode prior to gas purging are 8.84 and 21.04 $\times$ 10^{-8} kg s^{-1}, respectively. The inlet water fluxes are relatively smaller compared with the water flux with 90%RH of 65.6 $\times$ 10^{-8} kg s^{-1}, leading to the above peculiar phenomenon. The membrane water with different RHs is consistent with the equilibrium membrane water calculated by Eq. (22). It is suggested that the final membrane water content can be firstly predicted before the gas purging. From Fig. 13 it can be observed that the relative humidity should not be higher than 70% for the cold-start possibility as beyond which the final membrane water content is larger than 6.

Influence of the temperature (case 3)

Gas purging with high temperature can enhance the surface evaporation between the drying front and the purging gas. Fig. 14 shows the evolution curves of the volumetrically averaged membrane temperature and liquid water saturation with different gas inlet temperatures. As expected, the final

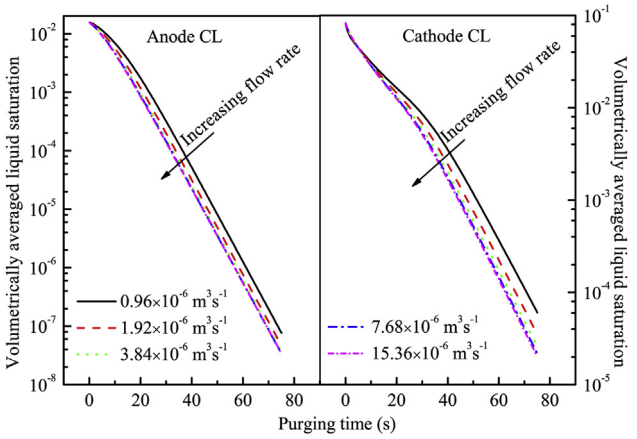

Fig. 9 – Evolutions of the volumetrically averaged liquid saturation in CLs with different gas flow rates

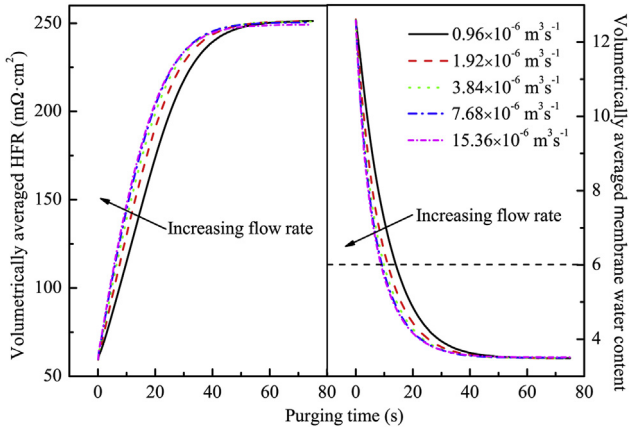

Fig. 10 – Evolutions of the volumetrically averaged HFR and membrane water content in MEM with different purging flow rates

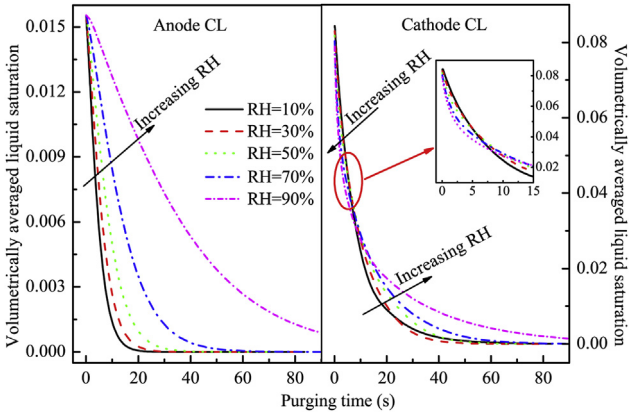

Fig. 11 – Evolutions of the volumetrically averaged liquid saturation in CLs with different relative humidity

membrane temperature increases with the purging temperature. It should be noted that the temperature of the current collectors is kept as 333 K during the whole gas purging process. The heat flux bringing into the cell is comparatively

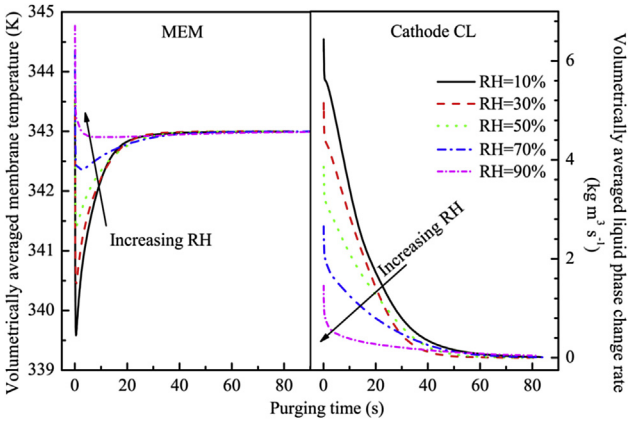

Fig. 12 – Evolutions of the volumetrically averaged membrane temperature and liquid phase change rate in cathode CL with different relative humidity

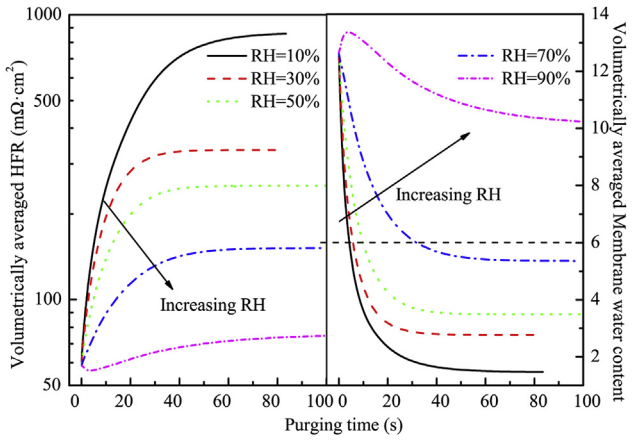

Fig. 13 – Evolution curves of the volumetrically averaged HFR and membrane water with different relative humidity in MEM

small and therefore the final membrane temperature only increases slightly. It is interesting that the dryness of the liquid saturation in cathode CL needs a longer purging time with a higher purging temperature. The reason is attributed to the fact that the inlet water flux increases significantly with a higher temperature under the same relative humidity. The inlet water fluxes are 15.34, 24.0, 36.46 and 53.89 $\times 10^{-8}$ kg s^{-1}, respectively. The evolution of the liquid saturation with the purging temperature for the first several seconds shows similar variation as observed in Fig. 11. Fig. 15 presents the evolution of the volumetrically averaged HFR and membrane water content. Similar result can be observed for the dryness of the membrane that it takes a longer time with a higher purging temperature. Besides, the final membrane water content increases with the purging temperature. Since the final membrane temperature only changes slightly with the purging temperature, the final membrane water content should be related with the inlet water flux. Tajiri and Wang [24] pointed out that the convective water flux $\frac{Q(p_{v,sat}-p_{v,inlet})}{RT_{in}A_{ch}}$ is a critical parameter to determine the overall dryness of the membrane. This assumption was based on the fact that the

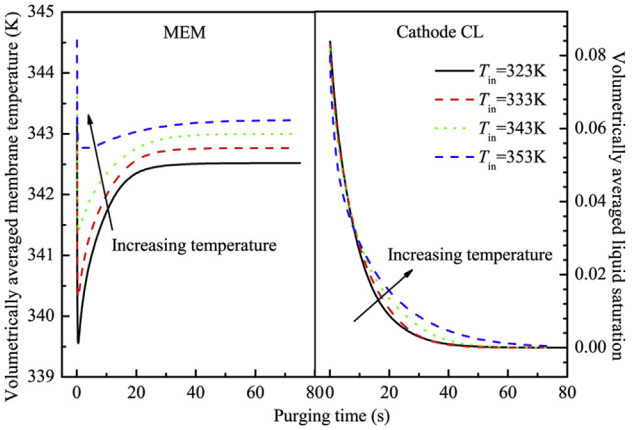

Fig. 14 – Evolutions of the volumetrically averaged membrane temperature and liquid water saturation in cathode CL with different purging temperature

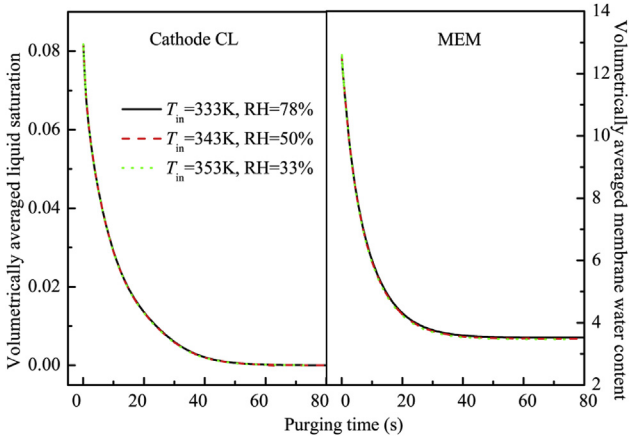

Fig. 16 – Evolutions of the volumetrically averaged liquid saturation in CCL and membrane water in MEM for three purging RHs with fixed inlet water flux.

outlet gas was kept fully humidified during the whole gas purging process. To numerically confirm this point, the inlet water flux for the purging temperature of 333 and 353 K as well as the gas flow rate are kept the same as the basic case and simulation were conducted for three RHs (within 78% and 33%). Fig. 16 presents the dryness of the liquid saturation in CCL and the membrane water in MEM with the same inlet water flux. The result indicates that for the fixed inlet water flux the evolution of the liquid saturation and membrane water are almost the same for the three combinations of T_{in} and RH, indicating that they are highly dependent on the overall inlet water flux other than the convective water flux with the same gas flow rate.

Evaluation of the operation parameters

The purge performance (such as the parasitic power, purge time and membrane water distribution) can be greatly influenced by the aforementioned operation parameters. During the purging process, the energy consumption and the uniformity of the membrane water content distribution are selected to evaluate the purging performance. Since the pressure drop of the gas channels is small, the compression power and the pumping power are neglected and only the energy for heating the purging gas from the ambient temperature T_{amb} is considered [29]. The energy consumption required for the purging gas W_{EC} is calculated as:

$$W_{EC} = 2\dot{m}c_p(T_{in} - T_{amb})t_{purge} \quad (37)$$

where c_p is the specific heat capacity purging gas. t_{purge} denotes to the purging time. T_{amb} is chosen as 298 K.

The maximum membrane water distribution uniformity is evaluated with the membrane water content variation ξ, which is described as

$$\xi = \lambda_{max} - \lambda_{min} \quad (38)$$

where λ_{max} and λ_{min} are the local maximum and minimum membrane water content at a certain volumetrically membrane water content.

Fig. 17 illustrates the energy consumption and the maximum membrane water content variation influenced by the operation parameters. The x-axis in Fig. 17(a) refers to the volumetrically averaged membrane water content during the gas purging. Though the dryness of the membrane can be enhanced with the increase of the gas flow rate slightly (see Fig. 10), the energy consumption increases significantly. This suggests that it is not economic to improve the purging effectiveness with high gas flow rate. With the increase of the relative humidity, the total purging time needed increases (see Fig. 13) and therefore the total energy consumption increases with the relative humidity greatly. It indicates that the inlet water flux for the dryness of the fuel cell should be kept low to guarantee the purging effectiveness. The energy consumption increases with the purging temperature since both the purging time and the temperature gradient for heating increase. Purging with high temperature should be avoided unless the corresponding relative humidity is low.

Fig.17(b) shows that the maximum membrane water content difference decreases with the increasing gas flow rate. As is addressed before, the gas flow rate benefits the dryness of the whole membrane and a larger water flux is also beneficial

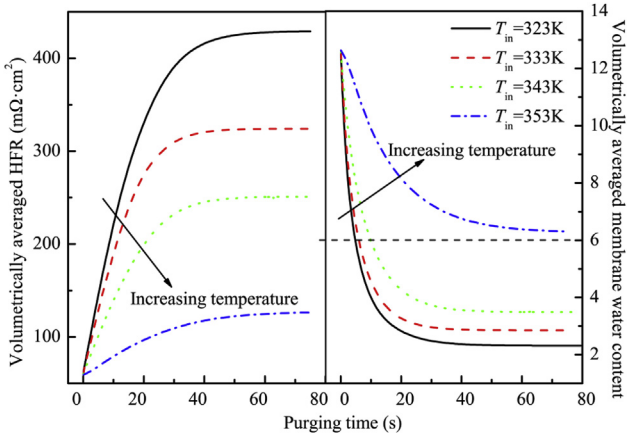

Fig. 15 – Evolutions of the volumetrically averaged HFR and membrane water content with different purging temperature

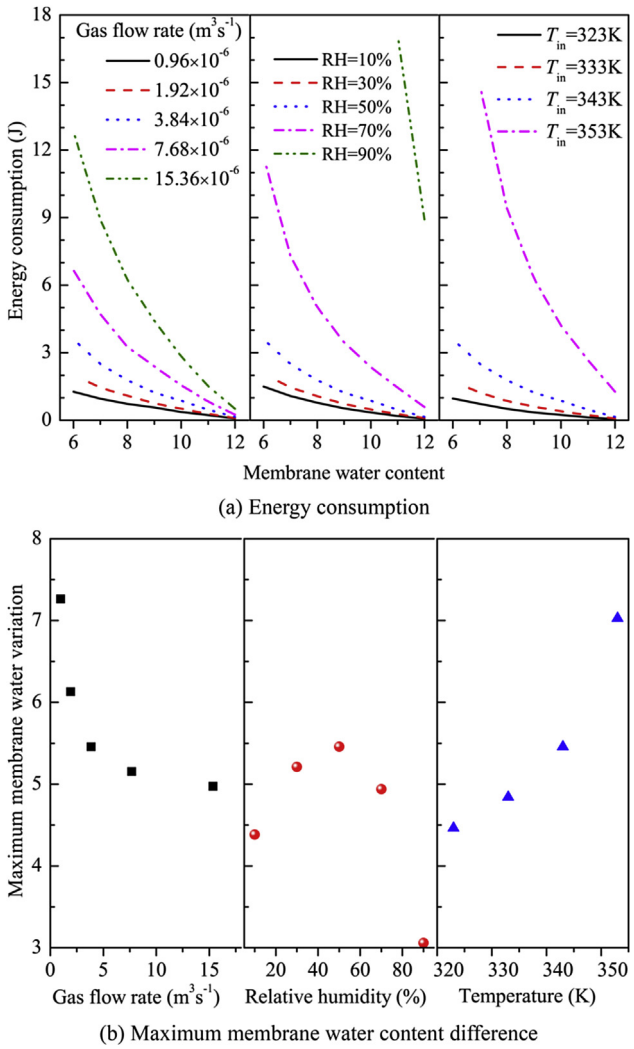

Fig. 17 – Influence of the operation parameters on the energy consumption and maximum membrane water content variation difference

for the uniformity of the membrane water distribution. The maximum membrane water difference increases firstly and then decrease with the relative humidity. The reason may be explained as follows. Though the minimum membrane water content decreases with low relative humidity, the drying rate of the whole membrane increases correspondingly and which may explain the low membrane water content difference with low relative humidity; when purging with high relative humidity, the increasing water flux and the overall membrane water content, together with the decreasing drying rate result in a low membrane water difference. The maximum membrane water content variation increases with the purging temperature since the drying rate decreases.

Conclusions

A transient purge model based on a two-fluid model is built to investigate the gas purging in a fuel cell. Parameters sensitivities (such as the gas flow rate, relative humidity and inlet temperature) are performed to study the water removal process. Evolution characteristics of the HFR have been predicted. The energy consumption and the maximum membrane water difference are adopted to investigate the purging performance. The main conclusions are as follows:

1. Water removal processes are not sequential, and the dryness of GCs is relatively easier compared with that of other sub-regions; the capillary driven flow is extremely small and thereby the main drying mechanism in porous medium is the surface evaporation; the membrane temperature decreases firstly and then increases back to the purging temperature; the variation of the membrane water content in membrane is similar to that of the liquid saturation in porous medium.
2. The overall dryness of the fuel cell improves slightly with the increase in gas flow rate since it is diffusion dominated; the final membrane water content is independent on the gas flow rate.
3. Purging with lower RH benefits the overall dryness of the fuel cell since the surface evaporation is highly related with RH; the final membrane water content can be predicted by the equilibrium equation before the gas purging since it is the equilibrium water that the membrane water content will finally reach.
4. Dryness of the liquid saturation in CCL needs a longer purging time with a higher purging temperature and the final membrane water content also increases with the purging temperature; the evolution of the liquid saturation and membrane water content highly depends on the overall inlet water flux other than the convective water flux with the same gas flow rate.
5. For the water removal under the pendular stage, purging with low gas flow rate is of efficient energy consumption and high non-uniformity in membrane water content; for low energy consumption and low non-uniformity in membrane water content, purging with low relative humidity and low temperature is suggested for certain cases in the present work.

Acknowledgment

This work is supported by the Key Project of the National Natural Science Foundation of China (51136004) and 111 Project (B16038).

REFERENCES

[1] Jiao K, Li X. Water transport in polymer electrolyte membrane fuel cells. Prog Energy Combust Sci 2011;37(3):221–91.
[2] Ge S, Wang C-Y. Characteristics of subzero startup and water/ice formation on the catalyst layer in a polymer electrolyte fuel cell. Electrochim Acta 2007;52(14):4825–35.
[3] Jiao K, Li X. Effects of various operating and initial conditions on cold start performance of polymer electrolyte membrane fuel cells. Int J Hydrogen Energy 2009;34(19):8171–84.

[4] Wang X, Tajiri K, Ahluwalia RK. Water transport during startup and shutdown of polymer electrolyte fuel cell stacks. J Power Sources 2010;195(19):6680–7.
[5] St-Pierre J, Roberts J, Colbow K, Campbell S, Nelson A. PEMFC operational and design strategies for sub zero environments. J New Mater Electrochem Syst 2005;8(3):163–76.
[6] Luo Y, Jiao K, Jia B. Elucidating the constant power, current and voltage cold start modes of proton exchange membrane fuel cell. Int J Heat Mass Transf 2014;77:489–500.
[7] Du Q, Jia B, Luo Y, Chen J, Zhou Y, Jiao K. Maximum power cold start mode of proton exchange membrane fuel cell. Int J Hydrogen Energy 2014;39(16):8390–400.
[8] Luo Y, Jia B, Jiao K, Du Q, Yin Y, Wang H, et al. Catalytic hydrogen–oxygen reaction in anode and cathode for cold start of proton exchange membrane fuel cell. Int J Hydrogen Energy 2015;40(32):10293–307.
[9] Song K-Y, Kim H-T. Effect of air purging and dry operation on durability of PEMFC under freeze/thaw cycles. Int J Hydrogen Energy 2011;36(19):12417–26.
[10] Kim SI, Lee NW, Kim YS, Kim MS. Effective purge method with addition of hydrogen on the cathode side for cold start in PEM fuel cell. Int J Hydrogen Energy 2013;38(26):11357–69.
[11] Nikiforow K, Karimäki H, Keränen TM, Ihonen J. Optimization study of purge cycle in proton exchange membrane fuel cell system. J Power Sources 2013;238:336–44.
[12] Strahl S, Husar A, Riera J. Experimental study of hydrogen purge effects on performance and efficiency of an open-cathode proton exchange membrane fuel cell system. J Power Sources 2014;248:474–82.
[13] Chen J, Siegel JB, Stefanopoulou AG, Waldecker JR. Optimization of purge cycle for dead-ended anode fuel cell operation. Int J Hydrogen Energy 2013;38(12):5092–105.
[14] Tsai S-W, Chen Y-S. A mathematical model to study the energy efficiency of a proton exchange membrane fuel cell with a dead-ended anode. Appl Energy 2017;188:151–9.
[15] Okedi TI, Meyer Q, Hunter H, Shearing PR, Brett DJL. Development of a polymer electrolyte fuel cell dead-ended anode purge strategy for use with a nitrogen-containing hydrogen gas supply. Int J Hydrogen Energy 2016. http://dx.doi.org/10.1016/j.ijhydene.2016.11.081.
[16] Abbou S, Dillet J, Maranzana G, Didierjean S, Lottin O. Local potential evolutions during proton exchange membrane fuel cell operation with dead-ended anode – Part I: impact of water diffusion and nitrogen crossover. J Power Sources 2017;340:337–46.
[17] Asghari S, Ashraf Khorasani MR, Dashti I. Investigation of self-humidified and dead-ended anode proton exchange membrane fuel cell performance using electrochemical impedance spectroscopy. Int J Hydrogen Energy 2016;41(28):12347–57.
[18] Cho KT, Mench MM. Coupled effects of flow field geometry and diffusion media material structure on evaporative water removal from polymer electrolyte fuel cells. Int J Hydrogen Energy 2010;35(22):12329–40.
[19] Cho KT, Mench MM. Effect of material properties on evaporative water removal from polymer electrolyte fuel cell diffusion media. J Power Sources 2010;195(19):6748–57.
[20] Cho KT, Mench MM. Fundamental characterization of evaporative water removal from fuel cell diffusion media. J Power Sources 2010;195(12):3858–69.
[21] Huang CLD. Multi-phase moisture transfer in porous media subjected to temperature gradient. Int J Heat Mass Transf 1979;22(9):1295–307.
[22] Sinha PK, Wang C-Y. Gas purge in a polymer electrolyte fuel cell. J Electrochem Soc 2007;154(11):B1158–68.
[23] Sinha PK, Wang C-Y. Two-phase modeling of gas purge in a polymer electrolyte fuel cell. J Power Sources 2008;183(2):609–18.
[24] Tajiri K, Wang C-Y, Tabuchi Y. Water removal from a PEFC during gas purge. Electrochim Acta 2008;53(22):6337–43.
[25] Shahidzadeh-Bonn N, Azouni A, Coussot P. Effect of wetting properties on the kinetics of drying of porous media. J Phys Condens Matter 2007;19(11):112101–7.
[26] Hao L, Yu H, Hou J, Song W, Shao Z, Yi B. Transient behavior of water generation in a proton exchange membrane fuel cell. J Power Sources 2008;177(2):404–11.
[27] Wang Y, Wang C-Y. Two-phase transients of polymer electrolyte fuel cells. J Electrochem Soc 2007;154(7):B636–43.
[28] Ito H, Maeda T, Kato A, Yoshida T, Ulleberg Ø. Gas purge for switching of Polymer electrolyte unitized reversible fuel cell. J Electrochem Soc 2010;157(7):B1072–80.
[29] Ding J, Mu Y-T, Zhai S, Tao W-Q. Numerical study of gas purge in polymer electrolyte membrane fuel cell. Int J Heat Mass Transf 2016;103:744–52.
[30] Jiang F, Wang C-Y. Numerical modeling of liquid water motion in a polymer electrolyte fuel cell. Int J Hydrogen Energy 2014;39(2):942–50.
[31] Hou J, Yu H, Yi B, Xiao Y, Wang H, Sun S, et al. Comparative study of PEM fuel cell storage at −20°C after gas purging. Electrochem Solid State Lett 2007;10(1):B11–5.
[32] Lee S-Y, Kim S-U, Kim H-J, Jang JH, Oh I-H. Water removal characteristics of proton exchange membrane fuel cells using a dry gas purging method. J Power Sources 2008;180(2):784–90.
[33] Kim YS, Kim SI, Lee NW, Kim MS. Study on a purge method using pressure reduction for effective water removal in polymer electrolyte membrane fuel cells. Int J Hydrogen Energy 2015;40(30):9473–84.
[34] Ye Q, Nguyen TV. Three-dimensional simulation of liquid water distribution in a PEMFC with experimentally measured capillary functions. J. Electrochem. Soc. 2007;154(12):B1242–51.
[35] Wu H, Berg P, Li X. Steady and unsteady 3D non-isothermal modeling of PEM fuel cells with the effect of non-equilibrium phase transfer. Appl Energy 2010;87(9):2778–84.
[36] Jiao K, He P, Du Q, Yin Y. Three-dimensional multiphase modeling of alkaline anion exchange membrane fuel cell. Int J Hydrogen Energy 2014;39(11):5981–95.
[37] Cao T-F, Mu Y-T, Ding J, Lin H, He Y-L, Tao W-Q. Modeling the temperature distribution and performance of a PEM fuel cell with thermal contact resistance. Int J Heat Mass Transf 2015;87:544–56.
[38] Ju H, Wang CY, Cleghorn S, Beuscher U. Nonisothermal modeling of polymer electrolyte fuel cells. J Electrochem Soc 2005;152(8):A1645–53.
[39] Udell KS. Heat transfer in porous media considering phase change and capillarity-the heat pipe effect [J]. Int J Heat Mass Transf 1985;28(2):485–95.
[40] Springer TE, Zawodzinski TA. Polymer electrolyte fuel cell model. J Electrochem Soc 1991;138(8):2334–43.
[41] Berg P, Lu DM, Djilali N. Water management in PEM fuel cells. J Electrochem Soc 2004;151(3):A341–53.
[42] Kaviany M. Principles of heat transfer in porous media. Springer Science & Business Media; 2012.
[43] Zhang FY, Yang XG, Wang CY. Liquid water removal from a polymer electrolyte fuel cell. J Electrochem Soc 2006;153(2):A225–32.